

Understanding the defect levels and photoluminescence in a series of bismuth-doped perovskite oxides: First-principles study

Bibo Lou^{1,2,3}, Jun Wen,⁴ Lixin Ning,⁵ Min Yin,^{1,*} Chong-Geng Ma,^{3,†} and Chang-Kui Duan^{1,2,6,‡}

¹Hefei National Laboratory for Physical Sciences at the Microscale and School of Physical Sciences, University of Science and Technology of China, Hefei 230026, China


²CAS Key Laboratory of Microscale Magnetic Resonance, University of Science and Technology of China, Hefei 230026, China

³School of Optoelectronic Engineering & CQIPT-BUL Innovation Institute, Chongqing University of Posts and Telecommunications, Chongqing 400065, China

⁴School of Electronic Engineering and Intelligent Manufacturing, Anqing Normal University, Anqing 246133, China

⁵Anhui Province Key Laboratory of Optoelectric Materials Science and Technology, Key Laboratory of Functional Molecular Solids, Ministry of Education, Anhui Normal University, Wuhu, Anhui 241000, China

⁶CAS Center for Excellence in Quantum Information and Quantum Physics, University of Science and Technology of China, Hefei 230026, China

 (Received 28 March 2021; revised 27 July 2021; accepted 23 August 2021; published 1 September 2021)

First-principles calculations using the hybrid density functional are carried out to study the defect levels and photoluminescence of bismuth doped in perovskites $RAIO_3$ ($R = Y, Gd, La$) and $LaBO_3$ ($B = Al, Ga, In$). Bismuth dopants are confirmed to be predominantly Bi^{3+} occupying the R site, i.e., Bi_R^0 ($R = Y, Gd, La$). The variation of the electron trap depth $Bi_R(0/-1)$ is shown mainly due to the shift of the conduction band, while the hole trap level $Bi_R(+1/0)$ shows the correlation with the shortest $R-O$ bond length in hosts. Based on the defect level diagram from the first-principles calculation, the transition types of excitation and emission are predicted. Among the systems considered, the lowest excited level that produces the photoluminescence is the $^3P_{0,1}$ levels of the $6s^16p^1$ configuration of Bi^{3+} , except for Bi^{3+} -doped $LaAlO_3$, which is the valence band to Bi^{3+} charge transfer state. The photoluminescence involving $^3P_{0,1}$ states shows similar Stokes shift in the series, and the excitation and emission energies exhibit almost linear correlation with the band gaps of hosts of a slope ~ 0.22 . Furthermore, our calculations show that there is no tendency of forming excessive Bi^{3+} pairs in all the five $RBO_3:Bi^{3+}$, while the $Gd^{3+}-Gd^{3+}$ coupling in $GdAlO_3$ provides a “bridge” for energy migration from an excited isolated Bi^{3+} ion to the Bi^{3+} pairs that are naturally present due to random distribution, leading to the 495-nm emission being observed uniquely in bismuth-doped $GdAlO_3$ among the series of systems considered. The results lay the basis for manipulating the trap levels and excitation and emission wavelengths in Bi^{3+} -doped perovskite oxides.

DOI: [10.1103/PhysRevB.104.115101](https://doi.org/10.1103/PhysRevB.104.115101)

I. INTRODUCTION

With the presence of the ns^2 lone pair, the photoluminescence of Bi^{3+} is sensitive to the ligand environments and spans from the ultraviolet to the green, which makes bismuth doping attractive for scintillator or phosphor applications [1–7]. Furthermore, bismuth doping is commonly employed to sensitize the lanthanide activators in phosphors or to provide electron and hole traps for persistent luminescence and storage phosphors [8,9]. For further optimization and improvement of Bi-doped materials, it is essential to explore the site occupancy, valence state, structure-related luminescence mechanisms, or trends that suit the spectra of Bi-doped phosphorescent systems [9–11]. Along these lines, the empirical model provided by Wang *et al.* [12] establishes a relationship

between energy levels of Bi^{3+} dopants and host environment. Dorenbos *et al.* constructed vacuum referred binding energy (VRBE) diagrams for $6s$ and $6p$ electrons of Bi^{3+} dopants in a wide range of hosts to facilitate designing trap levels [13].

In a series of Bi-doped perovskite hosts [3–6], including $RAIO_3$ ($R = Y, Gd, La$) and $LaBO_3$ ($B = Al, In, Ga$), the Bi-related excitation and emission were found to vary remarkably with R or B cations. In particular, the photoluminescence of $LaAlO_3:Bi$ exhibits a much larger Stokes shift than those in other hosts. $GdAlO_3$ shows similar chemical properties and band structure with $YAlO_3$, while the emission spectra of $GdAlO_3:Bi$ exhibit an extra strong redshifted broad band not observed in $YAlO_3:Bi$. In order to clarify the trends of trap depths and photoluminescence in a series of Bi-doped RBO_3 phosphors, as well as to assist the designing and optimization of Bi activated luminescence materials, a systematic first-principles calculation [14–16] is significant.

The first-principles calculation has recently been employed in studying and elucidating the excitation, relaxation, and emission processes of the Bi^{3+} activated phosphors including

*yinmin@ustc.edu.cn

†macg@cqupt.edu.cn

‡ckduan@ustc.edu.cn

the optical transitions of $^1S_0 \rightarrow ^3P_{0,1}$ inner Bi^{3+} (A band), the valence band to Bi^{3+} charge transfer (CT) transitions, or the Bi^{3+} to conduction band, i.e., metal-to-metal charge transfer (MMCT) transition [17]. In addition, the aforementioned abnormal redshifted broadband emission of Bi-doped GdAlO_3 has been tentatively assigned as Bi^{3+} pairs or clusters [3]. Although similar emissions have been recognized in several other hosts [18,19], little is known on the pair or cluster's formation and excited-state properties [19]. For transitions involving complex defects, the first-principles calculations have been widely utilized to investigate the donor-acceptor pairs [20–22] by studying their formation energies and defect levels in band gaps.

Herein, first-principles calculation is performed on studying the luminescent properties of Bi-doped RAlO_3 ($R = \text{Y, Gd, La}$) and LaBO_3 ($B = \text{Al, Ga, In}$). The methodology and the main results are presented in Sec. II and Sec. III, respectively. The geometric and electronic structures of the five pristine hosts are discussed in Sec. III A, and the intrinsic defects and site occupancy of Bi dopants are discussed in Sec. III B, where Bi is confirmed to be predominantly Bi_R^0 , i.e., Bi^{3+} occupying the R site ($R = \text{Y, Gd, La}$). Then, Sec. III C focuses on the properties of Bi^{3+} -related defect levels, and the trends of optical transition energies. Meanwhile, in Sec. III D, the emission processes of the Bi pair in GdAlO_3 will be clarified based on the obtained excited-state equilibrium structures and energy transfer processes.

II. METHODOLOGY

A. General parameter settings

The crystal structure of YAlO_3 , GdAlO_3 , LaGaO_3 , and LaInO_3 compound belongs to the orthorhombic distorted perovskite structure (space group No. 62, $Pnma$), with primitive cell containing four RBO_3 formulas [3], while LaAlO_3 belongs to the perovskite structure of space group $Pm-3m$ (No. 221) with primitive cell containing a single LaAlO_3 formula [5]. Simple defects in YAlO_3 , GdAlO_3 , LaGaO_3 , and LaInO_3 crystals were modeled using a $2 \times 2 \times 1$ defective supercell containing 80 atoms, but for LaAlO_3 , a $3 \times 3 \times 3$ defective supercell containing 135 atoms was adopted. As for Bi pairs in GdAlO_3 and YAlO_3 , a larger $2 \times 2 \times 2$ defective supercell containing 160 atoms was employed.

First-principles calculations were carried out with density-functional theory (DFT) by employing the Perdew-Burke-Ernzerhof revised for solids (PBEsol) [23] within generalized gradient approximation implemented in the Vienna *Ab initio* Simulation Package (VASP) [24,25]. For bismuth containing supercells, spin-orbit coupling (SOC) is important and has been included in the structure relaxation. Semicore electrons are explicitly treated for Gd ($5p^6 5d^1 6s^2$), Y ($4s^2 4p^6 4d^1 5s^2$), La ($5s^2 5p^6 5d^1 6s^2$), Al ($3s^2 3p^1$), O ($2s^2 2p^4$), Ga ($3d^{10} 4s^2 4p^1$), In ($4d^{10} 5s^2 5p^1$), and Bi ($6s^2 6p^3$) with the projector augmented wave pseudopotentials [26]. The cutoff energy was set to 520 eV and a $2 \times 2 \times 2$ k -point mesh was employed in PBEsol calculations. Electronic energy minimization is performed with a tolerance of 10^{-6} eV, while the force on each atom is converged within 0.01 eV/Å. The valence-band maximum

(VBM) alignment of the five hosts relative to the vacuum state was obtained by PBEsol calculations on a slab with a vacuum layer of ~ 20 Å along the a axis for the five hosts. The slab contains $4 \times 1 \times 1$ unit cells with 80 atoms for YAlO_3 , GdAlO_3 , LaGaO_3 , LaInO_3 and $6 \times 1 \times 2$ unit cells with 60 atoms for LaAlO_3 .

B. Formation energies of defects

The formation energy of a defect X in the charge state of q is defined as follows [27]:

$$E^f(X^q, E_F) = E_{\text{tot}}[X^q] - E_{\text{tot}}[\text{bulk}] - \sum_i n_i \mu_i + qE_F, \quad (1)$$

where $E_{\text{tot}}[X^q]$ and $E_{\text{tot}}[\text{bulk}]$ are, correspondingly, the total energies of defect X^q and pristine supercells, q is the total charge of the defective supercell, n_i is the change in the number of the atoms of X^q supercell relative to the pristine supercell, and μ_i is the corresponding chemical potential of the elements. The Fermi energy level E_F represents the chemical potential of the electrons. The thermodynamic charge transition level $\epsilon(q_1/q_2)$ is the value of E_F at which the formation energies of defect with two charge states, X^{q_1} and X^{q_2} , are equal. It can be deduced from Eq. (1) as

$$\epsilon(q_1/q_2) = \frac{E_{\text{tot}}(\{X^{q_1}\}) - E_{\text{tot}}(\{X^{q_2}\})}{q_2 - q_1}. \quad (2)$$

C. Charge corrections

Charge corrections are required in obtain the correct $E_{\text{tot}}[X^q]$ in Eq. (1) from the raw value of a supercell calculation and are obtained by including the combination of the Lany-Zunger image charge correction and the potential alignment ($q\Delta V$) correction by following Ref. [28]. More detailed descriptions are provided in the Supplemental Material (SM) [29]. The image charge interaction corrections of monovalence defects in $\text{RBO}_3:\text{Bi}$ are no more than 0.07 eV (Table S1 in the SM [29]). The negatively trivalent charged cation vacancies exhibit significant potential alignments (Fig. S1 in the SM [29]) and image charge interactions compared to other defects, which are consistent with the finite cell-size correction of LaAlO_3 performed by a linear fit [30]. The total charge corrections for cation vacancies as listed in Table S2 of the SM [29], while those of antisite defects and V_O^{2+} are less or about 0.1 eV in magnitude and are neglected in this work.

D. Excited-state equilibrium geometric structure

Generally, the most significant emission related to isolated Bi^{3+} in crystals originates from the equilibrium structure of the lowest one among the three types of excited states, i.e., MMCT state, CT state, and the A band ($^3P_{0,1}$) states. Based on our previous work [17], the equilibrium geometric structure of MMCT excited state was approximated as $\text{RBO}_3 : \text{Bi}_R^+$, which was obtained by the geometric relaxation of the system with one electron removed from the $\text{RBO}_3 : \text{Bi}_R^0$ supercell. Similarly, the equilibrium geometric structure of CT state was approximated by that of $\text{RBO}_3 : \text{Bi}_R^-$. The $^3P_{0,1}$ excited state was obtained by constraining the electron occupancy to $(6s_{1/2})^1(6p_{1/2})^1$ for $\text{RBO}_3 : \text{Bi}_R^0$, where $6s_{1/2}$ and $6p_{1/2}$ are Kohn-Sham (KS) orbitals obtained with PBEsol by including

SOC. The equilibrium geometric structures of the excited states of the Bi pairs in YAlO_3 and GdAlO_3 were obtained via structural relaxation for spin triplets, which turned out to be $\text{Bi}_R^- - \text{Bi}_R^+$ (referred to as $\text{Bi}^{2+} - \text{Bi}^{4+}$)-type charge transfer states.

E. Hybrid DFT calculations

Hybrid DFT, which mixes a portion (denoted by the parameter α) of Hartree-Fock exchange [31], has emerged as a useful method for more reliable calculations on the band structures and defect levels for many semiconductors and insulators. Appropriate hybrid density-functional calculations under the generalized Kohn-Sham (GKS) scheme yield GKS one-electron gaps that equal the fundamental gap [32]. The parameter weighted on the static electronic dielectric constant, $\alpha = 1/\epsilon_\infty$, has been shown to reproduce electronic structure in wide-gap oxide semiconductors [33]. Hence, we carried out hybrid DFT calculations on the geometric structures obtained with the methods in Sec. II A to obtain improved band gaps, defect levels, and excitation and emission energies for better comparison with experiments. The mixing parameter was determined by using the PBEsol-calculated ϵ_∞ as follows: $\alpha = 0.25$ for $\text{Y}(\text{Gd})\text{AlO}_3$, $\alpha = 0.23$ for LaAlO_3 , and $\alpha = 0.20$ for $\text{LaGa}(\text{In})\text{O}_3$. In hybrid DFT calculations, only one k point Γ was used to sample the Brillouin zone and the cutoff energy of the plane-wave basis was set to 400 eV.

F. Bi-related excitation and emission energies

Based on the Franck-Condon principle, the peak energy of excitation or emission for a given transition can be obtained approximately by the differences of the total energies of the excited and ground electronic state at the equilibrium geometric structure of the initial electronic states of the transition. As mentioned in previous work [17], the MMCT excitation energy can be approximated by the vertical energy difference of $(\text{Bi}_R^+ + e_{\text{CBM}})$ from the ground state of Bi_R^0 , i.e.,

$$\epsilon_{\text{MMCT}} = [\epsilon_{\text{CBM}} + E_{\text{tot}}(\{\text{Bi}_R^+\}_{3+})] - E_{\text{tot}}(\text{Bi}_{3+}). \quad (4)$$

Here the two total energies with subscript “3+” were calculated at the geometric structures of the ground state of Bi_R^0 (Bi^{3+}). The MMCT emission was calculated similarly but at the equilibrium structure of Bi_R^+ by neglecting the impact of the extra conduction band minimum (CBM) electron on the structure. In Eq. (4), since the total charge of the supercell is the same for initial and final states, the charge correction difference between them is neglected. Actually, the accuracy of the calculated band gap exhibits more influence on the errors of the MMCT or CT transition energies. Similarly, the CT excitation and emission energies can be calculated by the vertical energy difference between the system of $(\text{Bi}_R^- + h_{\text{VBM}})$ and of Bi_R^0 following the Franck-Condon principle, i.e.,

$$\epsilon_{\text{CT}} = [E_{\text{tot}}(\{\text{Bi}_R^-\}_{3+}) - \epsilon_{\text{VBM}}] - E_{\text{tot}}(\text{Bi}_{3+}). \quad (5)$$

For the excitation and emission energies of the A-band state and Bi pair, these transition energies were firstly obtained by the calculations employing the PBEsol functional both with and without including SOC, and then their difference was used as an estimation for the SOC contribution to correct the transition energy in hybrid DFT without including SOC.

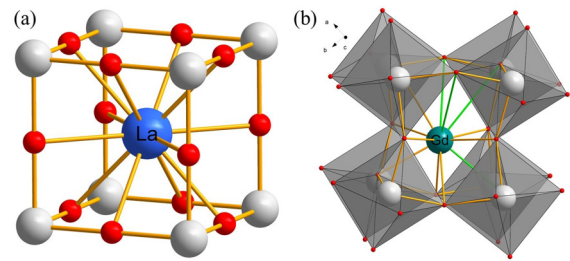


FIG. 1. Crystalline structures of the cubic perovskite LaAlO_3 (a), and the orthorhombic distorted perovskite (b) exemplified by GdAlO_3 .

III. RESULTS AND DISCUSSION

As a cubic perovskite, the La atoms of LaAlO_3 are located at Wyck. $1b$ sites in the center of 12 equivalent oxygen ligands, as shown in Fig. 1(a). For the other four $R\text{BO}_3$ perovskites, due to the smaller effective ion radii, the R cations are located at Wyck. $4c$ sites inside a distorted cube with inversion symmetry, as plotted in Fig. 1(b). There are four oxygen atoms whose bond lengths (in green) exceed 3 Å. In the following discussions, those four oxygen atoms with longer bond lengths are not counted as ligands of the R cations in distorted perovskites. The B cation is surrounded by six oxygen anions for all the perovskites. The equilibrium geometric structures of five pristine $R\text{BO}_3$ perovskites were firstly relaxed with PBEsol functional. The deviation between the calculated lattice parameters (Table S3 in the SM [29]) and the corresponding experimental values are mostly less than 0.4%. Thus, the PBEsol can well describe the lattice parameters.

A. Band structures of the five $R\text{BO}_3$ hosts

The Kohn-Sham gaps predicted by PBEsol functional are listed in Table I for the five perovskites, which show serious underestimation compared to these from the exciton creation energies or the host absorption spectra [34]. For the charge transfer transitions, the accuracy of the band gaps can greatly influence the spectra analysis. Experimentally, various intrinsic defects may bring difficulties in obtaining accurate optical band gaps; for example, the optical band gaps from the absorbance spectrum measurements were reported to be much smaller values of 5.70 eV in GdAlO_3 [35,36] and 5.85 eV in YAlO_3 [37]. Theoretically, the values are strongly dependent on parameter choices and a variety of values from 5.58 to 8.79 eV have been obtained [38,39]. The band gaps obtained

TABLE I. The DFT and hybrid DFT calculated band gaps for the five perovskites (in units of eV).

Band gap	YAlO_3	GdAlO_3	LaAlO_3	LaGaO_3	LaInO_3
PBEsol	5.63	5.35	3.46	3.68	2.87
Hybrid DFT	8.21	7.73	5.55	5.69	4.60
Expt. ^a	7.96	7.40	5.90	5.67	4.77

^aThe exciton creation energies from Refs. [34,49,50].

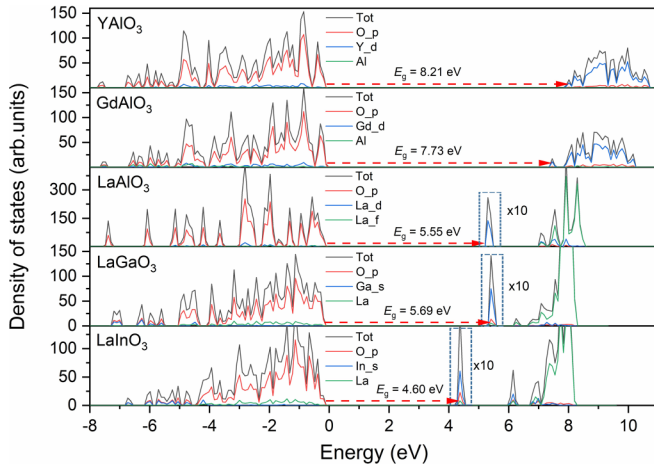


FIG. 2. The total or partial DOSs of the band edges for pristine hosts calculated with the hybrid DFT method. It is noted that the DOSs of the bottom of the conduction band in LaAlO_3 , LaGaO_3 and LaInO_3 are magnified by tenfold for better display.

with the hybrid DFT calculation here are compared to experiments in Table I, showing the significant improvement over PBEsol values and overall consistent with experiments.

The density of states (DOS) for the hosts obtained by the hybrid DFT (Fig. 2) shows that the top of the valence bands for all the five perovskites are dominated by the O- p orbitals. In the three RAIO_3 hosts, the compositions of conduction band are dominated by the d orbitals of R cations, while the Al atomic orbitals hardly contribute to the band-edge states. In LaAlO_3 , the conduction band between 7 and 9 eV above the VBM are dominated by the La- f orbitals. The La- f orbitals remain dominant in the higher conduction bands for LaGaO_3 and LaInO_3 ; however, the s orbitals of In^{3+} (Ga^{3+}) ions are lower than the La- d orbitals and thus dominating the properties of the CBM in those two hosts. For Gd^{3+} ion, it is difficult to add or remove a Gd- $4f$ electron; thus, its $4f$ electrons are placed in the core pseudopotential in this work and there are no $4f$ orbitals in the DOS of GdAlO_3 . Instead, the intra $4f$ - $4f$ transitions in Gd^{3+} ions are at about $32\,000\text{ cm}^{-1}$ and hardly influenced by the environment.

B. Intrinsic defects and site occupancy of Bi dopants in RBO_3

The site occupancy and valence states of luminescence center have usually been analyzed based on ionic radius, the valence states of host ions, and synthetic chemical atmosphere. It is noted that the relative abundance of elements may also play an important role [40,41]. The effective ionic radii of the Bi^{3+} ion (1.17 Å, coordination number CN = 8; 1.03 Å, CN = 6) are similar to those of Y^{3+} (1.02 Å, CN = 8), Gd^{3+} (1.05 Å, CN = 8), and La^{3+} (1.16 Å, CN = 8), and significantly larger than those of Al^{3+} (0.54 Å, CN = 6) and Ga^{3+} (0.62 Å, CN = 6). Thus, the incorporated Bi ions tend to substitute Y, Gd, and La cations in the form of Bi^{3+} in YAlO_3 , GdAlO_3 , and LaAl(Ga)O_3 , respectively. For LaInO_3 :Bi, the effective ionic radius of In^{3+} (0.80 Å, CN = 6) is only slightly smaller than that of Bi^{3+} ion with the same CN. Hence, it cannot be ruled out that Bi ions replace In^{3+} under favorable conditions. Therefore, we carried out calculations on the

formation energy polylines of Bi_R and Bi_B defects in the RBO_3 series to explore this as follows.

Figure 3 plots the formation energies of the intrinsic defects, including R or B cation vacancies (V_R or V_B), oxygen vacancies (V_O), and cation antisite defects (R_B or B_R), as well as those of Bi substituted the R or B ions (Bi_R or Bi_B). The employed chemical potentials were determined by considering fabrication conditions, and are subject to various constraints, such as $\mu_{\text{RBO}_3(\text{bulk})} = \mu_R + \mu_B + 3\mu_O$. Since the Bi-doped RBO_3 phosphors were sintered in air [3–6], the chemical potential of oxygen was determined as $\mu_O = \frac{1}{2}E_{\text{O}_2} + \Delta\mu_O$, where $\Delta\mu_O = -1.12\text{ eV}$ was estimated for the oxygen partial pressure (0.2 of the atmosphere pressure) at 1500 K. The enthalpy differences $\Delta H = \mu_{\text{RBO}_3(\text{bulk})} - \frac{1}{2}\mu_{\text{R}_2\text{O}_3(\text{bulk})} - \frac{1}{2}\mu_{\text{B}_2\text{O}_3(\text{bulk})} - 3\mu_O$ of material formation were obtained as -0.35 eV (GdAlO_3), -0.57 eV (LaAlO_3), -0.46 eV (LaGaO_3), and -0.18 eV (LaInO_3). As a reference, we adopted the intermediate chemical potentials of $\mu_{\text{R}_2\text{O}_3} = \mu_{\text{R}_2\text{O}_3(\text{bulk})} + \frac{1}{2}\Delta H$ and $\mu_{\text{B}_2\text{O}_3} = \mu_{\text{B}_2\text{O}_3(\text{bulk})} + \frac{1}{2}\Delta H$ in the calculation. Then the chemical potentials of the cations were obtained by $\mu_R = \frac{1}{2}(\mu_{\text{R}_2\text{O}_3} - 3\mu_O)$ and $\mu_B = \frac{1}{2}(\mu_{\text{B}_2\text{O}_3} - 3\mu_O)$. According to the formation energies diagrams, the most stable Bi dopant under the condition considered is Bi_R^0 ($R = \text{Y, Gd, La}$), i.e., Bi^{3+} replacing R ions in the host, Bi_R^- can exist in all the five hosts if the Fermi level is close to CBM, and Bi_R^+ can exist in the hosts other than LaAlO_3 if the Fermi level approaches VBM. In LaInO_3 :Bi, Bi can potentially occupy In^{3+} site in strong oxidization or excessive La_2O_3 conditions. However, under the ambient condition, the equilibrium Fermi level of LaInO_3 :Bi is determined by the charge neutrality of In_{La}^+ and $\text{V}_{\text{La}}^{3-}$ defects, and Bi_{La}^0 defect is about 0.6 eV more favorable in energy than $\text{Bi}_{\text{In}}^{0,1+}$. To sum up, the Bi_R^0 defects that are referred to as Bi^{3+} dopants are predominant in all the five perovskites, and in the following sections we will mainly focus on the study of defect levels and photoluminescence related to Bi_R^0 (Bi^{3+}).

In the four distorted perovskites, the cation vacancies turn out to be the dominate intrinsic defects to neutralize the minor amount of Bi_R^+ , while for LaAlO_3 :Bi, Bi_{La}^+ is unstable and the equilibrium Fermi energy is determined by the Schottky vacancies of V_O^{2+} and $\text{V}_{\text{La}}^{3-}$. The In^{3+} ion shows a slightly smaller effective ionic radius than that of the Bi^{3+} ion in LaInO_3 :Bi and the coordinate environment of In^{3+} site is appropriate for Bi_{In}^+ defect; thus, the formation energy of Bi_{In}^+ is lower than that of Bi_{La}^+ at a given Fermi level, and the charge balance is provided by Bi_{In}^+ defect and cation vacancies in LaInO_3 :Bi. For a small amount of intrinsic defects in RBO_3 :Bi, the cation vacancies are the most important and their $(-2/-3)$ transition levels are close to the VBM. In hybrid DFT calculations, they are about 1.0 eV above the VBM. The details can be found in Table S4 of the SM [29]. Those shallow potential electron or hole traps may serve as trap centers for excitation energy or act as host lattice quenching centers, which may influence the performance of phosphors. However, the trends of defect levels and the optical transition energies of Bi^{3+} are independent of those intrinsic defects.

Due to the difference of the effective ionic radius, the substitution of R cations by Bi ions increases the mean distances of R -O in GdAlO_3 and YAlO_3 , but is opposite in LaGaO_3

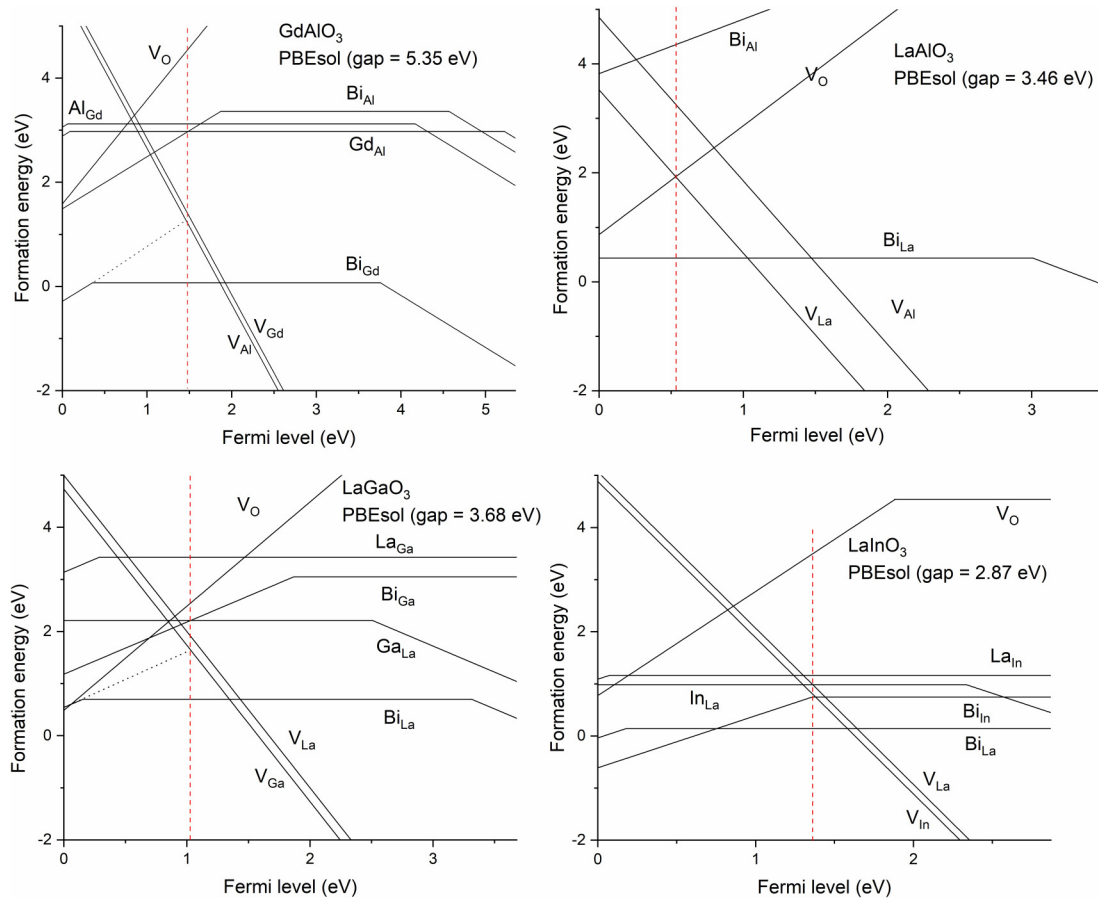


FIG. 3. Formation energies of intrinsic defects and Bi_R or Bi_B defects as a function of the Fermi level for the five perovskites in O-rich environment calculated with PBEsol. The properties of intrinsic defects in YAlO_3 are close to GdAlO_3 due to the similar electronic structures, and are omitted. The vertical dashed lines show the Fermi energies determined by charge equilibrium between the two major oppositely charged defects. It is noted that $\Delta\mu_{\text{Bi}} = 0$ was adopted and SOC was included in the $(-1/0)$ transition level calculation. The formation energy polylines of Bi_R or Bi_B defects are subject to a minor upshift to suit the actual doping concentration.

and LaInO_3 (Table S5 of the SM [29]). The local structures of Bi_R^0 in excited states are different from that in the ground state due to changes in electron occupancy. In Fig. 4, the charge distributions are plotted for the distorted and cubic perovskites, including charge-density profiles of the nominal Bi-6s orbitals and Bi-6p orbitals in two systems. Figure 4(a) shows that nominal Bi-6s orbital contains substantial contributions from the 2p orbitals of the nearest four oxygen ligands in the distorted perovskites ($\text{GdAlO}_3:\text{Bi}$ are plotted for example). However, for the cubic perovskite $\text{LaAlO}_3:\text{Bi}$, the spatial distribution of the nominal Bi-6s is very scattered and the 12 oxygen ligands contribute equally. It is noted that the Bi-6s orbital is actually an antibonding orbital, and the orbital with dominant 6s character of the Bi ion is deep in the valence band.

The equilibrium geometric structures of the potential emission states (MMCT, CT, and $^3P_{0,1}$ states) were obtained for the Bi-doped distorted perovskites. And, the mean bond lengths are listed in Table S5 of the SM [29]. It is noted that the nominal Bi-6s orbital of $\text{LaAlO}_3:\text{Bi}$ is lower in energy than the VBM. Thus the $^3P_{0,1}$ or MMCT excited states cannot be obtained by the same methods as in the distorted perovskites. Compared with the ground state, the equilibrium structures of the excited states show clear changes in the mean

bond length of Bi-O (Table S6 of the SM [29]). Different from the overall variation of all the Bi-O bond lengths in

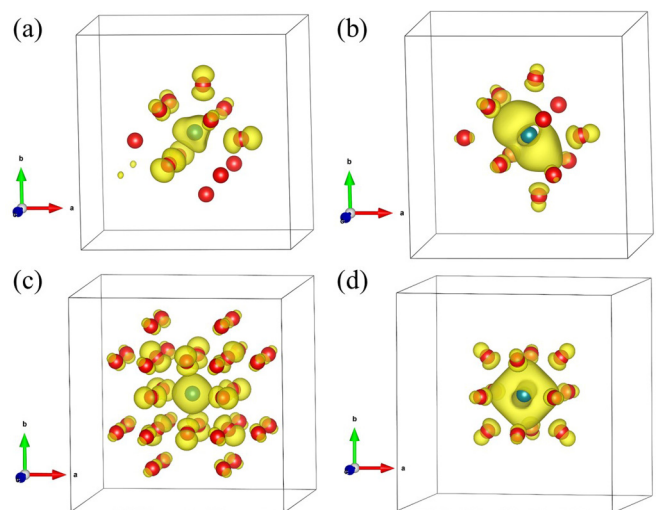


FIG. 4. The charge-density profiles of: Bi-6s KS orbital of Bi_R^0 in GdAlO_3 (a) and LaAlO_3 (c); Bi-6p KS orbitals of Bi_R^- in GdAlO_3 (b) and LaAlO_3 (d).

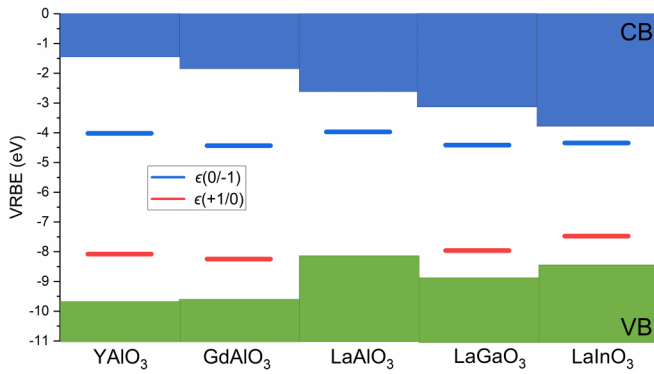


FIG. 5. Locations of the defect levels in the band gap for Bi^{3+} -doped five perovskites, where the band is aligned by the vacuum level.

different geometric structures in LaAlO_3 , there are four oxygen ligands whose bond lengths change more pronouncedly in those distorted perovskites. The lowest $6p$ KS orbitals in the distorted $R\text{BO}_3 : \text{Bi}_R^+$, as shown in Figs. 4(b) and 4(d), contain much less contributions from ligands than those of $6s$ KS orbitals. It is noted that the lowest $6p$ orbitals are degenerated in energy in LaAlO_3 due to the high symmetry, while those in the distorted perovskites are pointing along the direction with looser ligand environment. Meanwhile, the oxygen ligands, along the direction of the lowest $6p$ orbital, show larger relaxations in different excited states. Due to the large band gap in GdAlO_3 and YAlO_3 , the equilibrium geometric structures of the CT excited state ($\text{Bi}_R^- + h_{\text{VBM}}$) can be obtained by PBEsol or by PBEsol + SOC methods. It is interesting that the local structures obtained whether SOC is considered or not are quite similar, with the difference in the average bond length less than 0.01 \AA (Table S7 of the SM [29]). In structure relaxation, the SOC hardly influences the equilibrium geometric structures of Bi dopants in the distorted perovskite oxides.

C. Charge transition levels and optical transitions of isolated Bi^{3+} dopants

The calculated thermodynamic charge transition levels $\epsilon(+1/0)$ and $\epsilon(0/-1)$ of Bi_R relative to band edges are plotted in Fig. 5 for the five perovskites, where the VRBEs of electrons on VBM are -9.66 , -9.58 , and -8.18 eV for YAlO_3 , GdAlO_3 , and LaAlO_3 , respectively. The details can be found in Table S8 and Fig. S2 of the SM [29]. These are quite close to -9.04 , -8.66 , and -7.85 eV obtained by applying the chemical shift model for $R = \text{Y}$, Gd , and La , respectively [42]. It is noted that the hybrid DFT calculated depths of the hole or electron traps are independent of the alignment.

The hybrid DFT calculated $\epsilon(0/-1)$ levels of Bi_R defects are all lower than the CBM in the five hosts, and their values relative to CBM are, correspondingly, -2.57 , -2.59 , -1.34 , -1.24 , and -0.54 eV for YAlO_3 , GdAlO_3 , LaAlO_3 , LaGaO_3 , and LaInO_3 with inclusion of the charge corrections (Table S9 of the SM [29]). In experiment, the energy positions of the Bi- $6s$ and $-6p$ electrons of $\text{YAlO}_3:\text{Bi}$ were estimated to be about 2.0 eV relative to the band edges [42] by the spectroscopy studies of the excitation energies of the MMCT and

A-band states. For the listed five $R\text{BO}_3$ -type perovskites, the potential electron traps are dominated by the Bi- $6p$ orbitals and the VRBEs are all around -4.0 eV, similar to the cases in $\text{CaMO}_3:\text{Bi}$ ($M = \text{Zr}, \text{Sn}, \text{Ti}$) [17]. However, the VRBEs of the CBM in the five hosts vary from -1.5 to -3.8 eV, leading to very different electron trap depths in the above-mentioned five hosts, and even inexistence of Bi_{Ca} electron traps in CaTiO_3 and CaSnO_3 at all. Hence, the difference in electron trap is mainly due to the shift of the conduction band. This is consistent with the relatively flat variation of the lowest state of $6s6p$ configuration ($^3P_{0,1}$) in different hosts as reported in Ref. [18].

The $\epsilon(+1/0)$ transition levels of Bi_R defects in YAlO_3 , GdAlO_3 , LaGaO_3 , and LaInO_3 are above the VBM with depths of 1.58 , 1.33 , 0.91 , and 0.93 eV, respectively. However, their corresponding VRBEs vary dramatically from one to another host. The Bi_R defects can act as potential hole traps in all the hosts considered, except for LaAlO_3 , whose highest KS orbital that contains the Bi- $6s$ component is lower than the VBM and the monovalent charged defect Bi_{La}^+ is unstable. Since the hole trap involves the antibonding orbital of Bi- $6s$ mixed with oxygen ligands, we explore the relationship between the trap depth and the shortest $\text{Bi}_R\text{-O}$ or $R\text{-O}$ bond lengths for a series of perovskites (Table S10 in the SM [29]). It is interesting that the hole trap depths exhibit more obvious trends with the variation of $R\text{-O}$ bond lengths [Fig. 6(a)] than those of $\text{Bi}_R\text{-O}$ (not plotted). For the bond $R\text{-O}$ length increasing from 2.1 to 2.4 \AA , the hole trap depths decrease from 1.58 to 0.91 eV. The $R\text{-O}$ bond lengths reflect the influence of chemical environment on the antibonding orbital except for the bond length. This trend supports the centroid shift model [43] that relates the properties of Bi- $6s$ and Bi- $6p$ states with nephelauxetic effect [44], which becomes stronger with the shortening of the $R\text{-O}$ bond length.

As holes and electrons traps are significant in persistent and storage phosphors, the rule of the trap depth revealed in the discussion above can be adopted to manipulate their depths by varying host composition via solid solution or codoping of different ions. Meanwhile, the optical transition processes and energies of Bi activators can be predicted from the properties of the defect levels. For distorted perovskites, the transition level $\epsilon(+1/0)$ of Bi_R is above the VBM, so Bi_{La}^0 (Bi^{3+}) can catch the hole leaving behind by charge transfer excitation to form $^3P_{0,1}$, favoring in energy the intra- Bi^{3+} emission over the charge transfer emission. For Bi_{La}^0 (Bi^{3+}) in LaAlO_3 , the electrons near VBM greatly outnumbered those on the Bi- $6s$ orbital to counteract the smaller orbit overlap with $6p$ or the smaller electric dipole moment for the former. Hence, the CT excitation is presumably dominant in the excitation spectrum. The energy differences between VBM and $\epsilon(0/-1)$ are consistent with the energies of the adiabatic CT transitions. Similarly, the adiabatic MMCT transitions can be predicted by the energy differences between CBM and $\epsilon(+1/0)$.

Figure 6(b) plots the optical transition energies of Bi^{3+} ions in the five hosts obtained by the hybrid DFT calculation along with those reported experimental results, and the detailed data are listed in Table II. The calculated excitation and emission energies show great consistency with the measured ones. For the distorted perovskites, both the excitation and the emission are calculated to be dominated by the A-band transitions. The

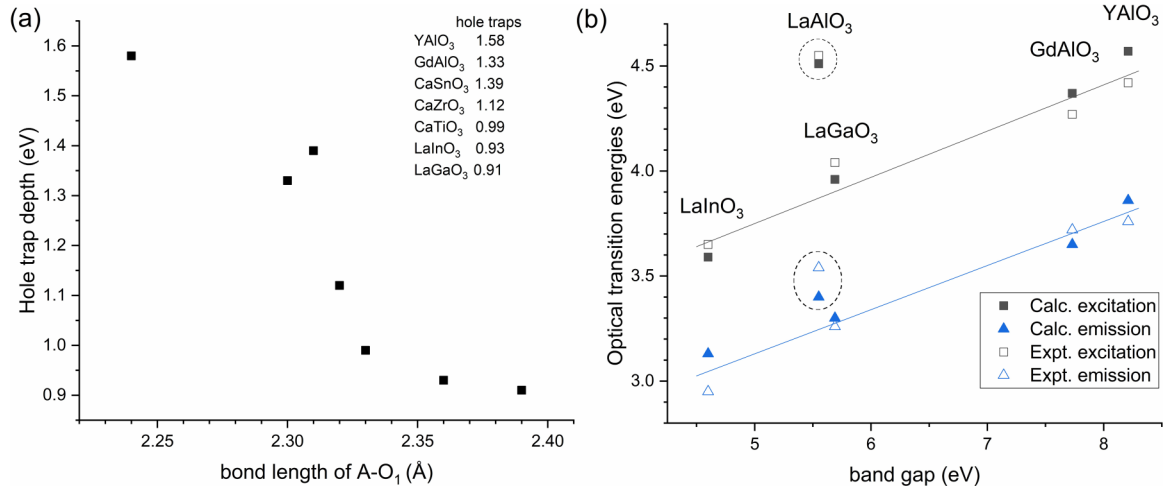


FIG. 6. (a) Relationship between the calculated hole trap depth and the calculated bond length of R cations and the nearest oxygen ligand in a series of perovskite oxides. (b) Calculated excitation and emission energies and the peaks in the measured bands of $\text{Bi}_R^0(\text{Bi}^{3+})$ in five hosts. The transitions are $\text{Bi-}6s^* \leftrightarrow \text{Bi-}6p$ ($^1S_0 \leftrightarrow ^3P_{0,1}$) type and are commonly referred to as A band in experiments, except for $\text{LaAlO}_3:\text{Bi}$, which is charge transfer from valence band to $\text{Bi-}6p$ orbital ($^1S_0 \leftrightarrow ^2P_{3/2} + \text{hole}$) type. The lines to show the trend have a slope of 0.22.

CT and MMCT excitations require a high energy and they have not been observed experimentally. For the A -band transition of Bi dopants in $R\text{BO}_3$, the SOC dominates the splitting [45] of $6s6p$ excited state as plotted in Fig. 7(b), where the difference in GKS values of B and C reflects SOC superposed with the effect of Coulomb exchange interaction and the crystal-field splitting. The DOS obtained without including SOC in Fig. 7(a) shows the crystal-field splitting of three $6p$ orbitals, while the difference between major and minor spins is due to Coulomb exchange interaction. Meanwhile, Fig. 6(b) shows that the A -band optical transition energies are linearly correlated to the band gaps with a small slope of ~ 0.22 , and the Stokes shifts are all ~ 0.7 eV. The excitation and emission of Bi^{3+} in LaAlO_3 are calculated to originate from the CT transitions, and the Stokes shift is calculated as 1.10 eV, which

is remarkably different from the transition energies in the other four $R\text{BO}_3:\text{Bi}^{3+}$. The calculated excitation and emission energies of $\text{LaAlO}_3:\text{Bi}^{3+}$ are consistent with the measurement well and can be utilized to correct the assignment of the spectra recorded in experiment [5]. Furthermore, the calculated MMCT excitation energy of 6.68 eV in $\text{YAlO}_3:\text{Bi}^{3+}$ can be utilized to assign the reported broad excitation band located at $E > 6.0$ eV, which is consistent with the estimation of the MMCT transition at approximately 6.5 eV in Ref. [18]. For $\text{GdAlO}_3:\text{Bi}^{3+}$, the calculated A -band excitation and emission energies of 4.37 and 3.65 eV match well with the measurements, but there is no other transition of the isolated Bi^{3+}

TABLE II. Calculated and measured transition energies (in units of eV) of Bi^{3+} (isolated Bi_R^0) ($R = \text{Y, Gd, La}$) in the five perovskites. Ex. and Em. stand for excitation and emission, respectively.

		A band		MMCT		CT	
		Ex.	Em.	Ex.	Em.	Ex.	Em.
YAlO ₃	Calc.	4.57	3.86	6.84	(6.05) ^a	6.43	(4.71)
	Expt.	4.42	3.76				
GdAlO ₃	Calc.	4.37	3.65	6.68	(5.96)	5.94	(4.30)
	Expt.	4.27	3.72	6.50			
LaAlO ₃	Calc.					4.51	3.40
	Expt.					4.55	3.54
LaGaO ₃	Calc.	3.96	3.30				
	Expt.	4.04	3.26				
LaInO ₃	Calc.	3.59	3.13				
	Expt.	3.65	2.95				

^aThe MMCT and CT excited states of $\text{Y}(\text{Gd})\text{AlO}_3:\text{Bi}$ are not actually emissive, as the excitations will relax to low-lying A -band excited states. Hence, the predicted emission energies are included in listed in parentheses.

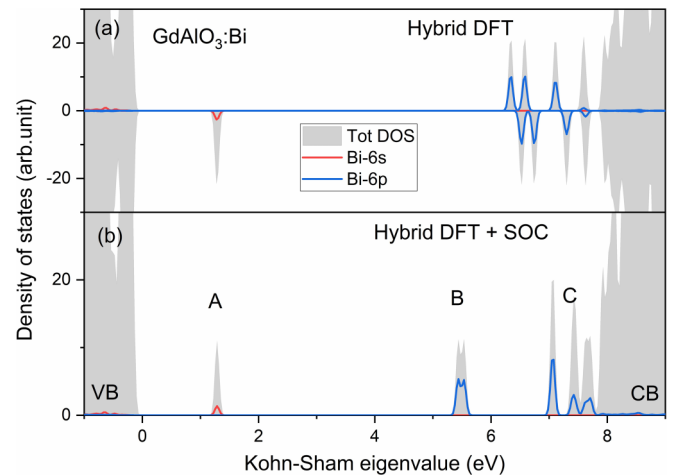


FIG. 7. The VBM referred GKS orbital energies of the system $\text{GdAlO}_3:\text{Bi}$ calculated with the (a) hybrid DFT and (b) hybrid DFT + SOC methods for an approximation of the $6s6p$ electron configuration. The DOSs calculated on the equilibrium geometric structure of $\text{GdAlO}_3:\text{Bi}$ when one electron is removed from the supercell. The valence band and one $6s_{1/2}$ orbital of GKS energy lower than VBM are occupied, while the other $6s_{1/2}$ (A), two $6p_{1/2}$ (B), and four $6p_{3/2}$ (C) orbitals are unoccupied.

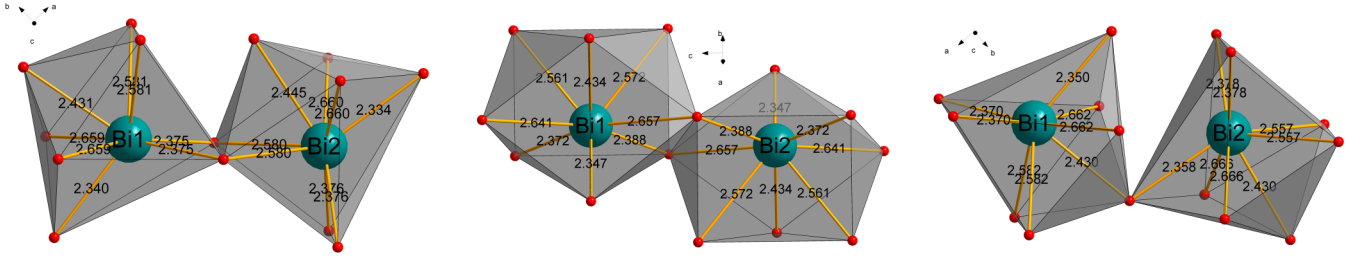


FIG. 8. Three types of Bi^{3+} pairs with different Bi^{3+} - Bi^{3+} distances of 3.724, 3.779, and 3.844 Å.

responsible for the dominating broad emission of 480 nm (2.58 eV), which will be discussed in detail below.

D. Properties of the Bi^{3+} pair in GdAlO_3 or YAlO_3

In 2017, Srivastava *et al.* assigned the visible emission band in $\text{GdAlO}_3:\text{Bi}$ to pairs or clusters of Bi^{3+} ions in the host lattice because of the strong dependence of the visible band intensity on the concentration of Bi dopants [3]. It is interesting that such pair-related luminescence is dominant in GdAlO_3 even at the doping levels of 0.5 at. % Bi sample, but has not been observed in YAlO_3 . It has been proposed that the unique pair emission is caused by the stronger interaction between Bi ions in GdAlO_3 [3], but little is known on the mechanism leading to the luminescence of Bi-related dimers or larger clusters in solids [19]. In order to explore the Bi pair formation in both GdAlO_3 and YAlO_3 , we calculated the pair-binding energies defined as $E_B = E^f[\text{Bi}_R^0 \text{ pair}] - 2 \times E^f[\text{Bi}_R^0]$ ($R = \text{Gd}$ or Y), which are listed in Table III. The relative concentration of Bi_R^0 pairs is related to that of Bi by $c(\text{Bi}_R^0 \text{ pair}) = \frac{1}{2} N c(\text{Bi}_R^0)^2 \exp[-E_B/(k_B T)]$, where $N = 6$ is the number of neighboring R cations of Bi_R ($R = \text{Gd}$ or Y), T is the temperature of thermal equilibrium distribution of Bi dopants, and $c(\text{Bi}_R^0 \text{ pair})$ and $c(\text{Bi}_R^0)$ are relative to the concentration of $R = \text{Gd}$ or Y in the hosts. Table III shows that all the binding energies are essentially zero, i.e., there is no attractive or repulsive interaction between two neighboring Bi ions, and no tendency of forming excessive Bi_R^0 (Bi^{3+}) pairs over those due to random distribution. The cases for LaAlO_3 , LaGaO_3 , and LaInO_3 are similar (data not listed). For example, for $c(\text{Bi}_{\text{Gd}}^0) = 0.50$ at. % in experiment, the concentration of Bi_{Gd}^0 pair is 0.0075 at. % of the number of Gd site or 1.5% of the concentration of Bi dopants.

In the distorted perovskite GdAlO_3 , there are three inequivalent adjacent Gd^{3+} ions around the isolated doped Bi_{Gd} and thus three different types of Bi^{3+} pairs need to be considered. Ground-state structure relaxations were carried out for all the three type of pairs, and the resultant Bi-Bi distances are, correspondingly, 3.724 Å (pair 1), 3.779 Å (pair 2), and 3.844 Å (pair 3), as plotted in Fig. 8, and two Bi atoms in

TABLE III. PBEsol calculated binding energies of Bi pairs at different distances.

	GdAlO_3			YAlO_3		
Bi-Bi distance (Å)	3.724	5.075	8.329	3.678	5.002	8.220
Binding energy (eV)	-0.012	0.002	0.003	-0.024	0.002	0.004

a pair are referred to as Bi_1 and Bi_2 . Only pair 2 has the space-inversion symmetry to interchange Bi_1 and Bi_2 . Since the oxygen environments of Bi and the Bi-Bi distances are similar in all three pairs, the excited-state properties and the transition energies are not expected to vary greatly with the slight difference of the distances between the two Bi_{Gd} defects in general.

In the excited states of pair 1 and pair 3, by setting the spin multiplicity $2S + 1 = 3$ in PBEsol calculations, an electron is lifted from the Bi-6s orbital of one Bi to the Bi-6p orbital of the other Bi to form the nominal $\text{Bi}_R^+ - \text{Bi}_R^-$ excited state. This is the difference from lifting an electron from Bi-6s to Bi-6p in a single Bi to form $^3P_{0,1}$ states. Figure 9 plots the hybrid DFT calculated partial charge density of the Bi pair ground state and the $\text{Bi}_R^+ - \text{Bi}_R^-$ excited state, showing clearly the intervalence charge transfer from Bi_1 to Bi_2 . Meanwhile, when the structure relaxations in pair 1 and pair 3 are performed by starting with Bi_1 being at the equilibrium geometric configuration of Bi_R^- or Bi_R^+ , we obtain two different excited-state equilibrium structures: with Bi-Bi distances of 3.624 Å ($\text{Bi}_{R1}^- - \text{Bi}_{R2}^+$) and 3.907 Å ($\text{Bi}_{R1}^+ - \text{Bi}_{R2}^-$) for pair 1, and 3.907 Å ($\text{Bi}_{R1}^- - \text{Bi}_{R2}^+$) and 3.548 Å ($\text{Bi}_{R1}^+ - \text{Bi}_{R2}^-$) for pair 3.

Due to the space-inversion symmetry in pair 2, the excited state (Bi-Bi^*), where the occupied major spin orbital of the Bi-6p type and the unoccupied minor spin orbital of the Bi-6s type are both contributed equally by the two Bi ions, is obtained naturally by setting the spin multiplicity $2S + 1 = 3$ in PBEsol calculations and Bi-Bi distance is 3.472 Å (Table S11 in the SM [29]). By setting the starting equilibrium geometric structures to break the inversion symmetry, the $\text{Bi}_R^- - \text{Bi}_R^+$ -type excited state is obtained in pair 2 with Bi-Bi distance of 3.776 Å, whereas the $\text{Bi}_{R1}^- - \text{Bi}_{R2}^+$ shows the same properties with $\text{Bi}_{R1}^+ - \text{Bi}_{R2}^-$. In contrast, there is no space inversion in

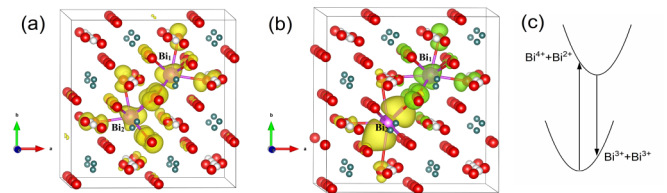


FIG. 9. The spin partial charge-density contours: (a) of the electrons in the outermost orbit of the ground state of the Bi pair in GdAlO_3 ; (b) of the excited state of Bi^{3+} pair in GdAlO_3 , where the yellow contour is the electron in the outermost orbit of major spin and the green contours is the hole in the outermost orbit of minor spin. (c) Schematic Bi^{3+} pair transitions in $\text{GdAlO}_3:\text{Bi}$.

TABLE IV. The energies (in units of eV) of various excited states of Bi pairs in GdAlO₃:Bi relative to their corresponding ground states.

	Pair 1		Pair 2			Pair 3	
	$\text{Bi}_R^- - \text{Bi}_R^+$	$\text{Bi}_R^+ - \text{Bi}_R^-$	$\text{Bi}_R^- - \text{Bi}_R^+$	(Bi-Bi)*	$\text{Bi}_R^+ - \text{Bi}_R^-$	$\text{Bi}_R^- - \text{Bi}_R^+$	$\text{Bi}_R^+ - \text{Bi}_R^-$
DFT	4.01	3.86	4.01	3.99	4.01	3.91	3.93
DFT + SOC	3.58	3.46	3.58	3.57	3.58	3.50	3.53
DFT + U	4.06	3.93	4.06	4.14	4.06	3.97	3.98
Hybrid DFT	4.33	4.16	4.41	4.59	4.41	4.26	4.32

pair 1 and pair 3, and the excited state (Bi-Bi)* is not obtained in PBEsol structural relaxation and it is unlikely to be stable.

Since the system energies of the ground state are almost equal in all the three kinds of pairs, the zero phonon transition energies (Table IV) with respect to the corresponding ground state are utilized to study the energies of various Bi³⁺-pair excited states and the interaction between two Bi sites. In pair 1, the energy of $\text{Bi}_{R1}^+ - \text{Bi}_{R2}^-$ excited state is 0.15 eV lower than the $\text{Bi}_{R1}^- - \text{Bi}_{R2}^+$ state in PBEsol calculation, although the Bi-Bi distance of $\text{Bi}_{R1}^+ - \text{Bi}_{R2}^-$ is longer (Table S11 in the SM [29]). However, the difference between those two types of charge transfers in pair 3 is negligible. Here, it turns out that the distance between Bi_R^- and Bi_R^+ is not the critical factor for the excitation energy. With the inclusion of SOC in PBEsol calculations, the system energies all decrease by about 0.4 eV in various excited states. For pair 2, the PBEsol calculated energy of the (Bi-Bi)* excited state is close to that of the $\text{Bi}_R^- - \text{Bi}_R^+$ state. The hybrid DFT calculation favors $\text{Bi}_R^- - \text{Bi}_R^+$ states in energy, similar to the DFT + U results. Considering the delocalization error in the results obtained by a conventional density functional such as PBEsol, it can be inferred that the most stable excited states for all the three Bi³⁺ pairs are actually $\text{Bi}_R^- - \text{Bi}_R^+$ type. The emission energies are around 2.6 eV from the lowest excited states of three pairs in hybrid DFT calculations.

Following the Franck-Condon principle, the excitation energy of Bi pair in GdAlO₃:Bi is calculated on the geometric structure of the ground state. In hybrid DFT calculations, the excitation energy of charge transfer transition between two Bi ions requires higher energy than intra-Bi excitation in all three types of Bi pairs. An empirical model has been developed in Ref. [19] to estimate the Bi pair transition and to calculate the lowest-lying excitation energy of $\text{Bi}_{R1}^0 - \text{Bi}_{R2}^0 \rightarrow \text{Bi}_R^- - \text{Bi}_R^+$ intervalence charge transfer transitions in oxidic compounds. They also note that the excitation bands of the A band and the Bi pair largely overlap in GdAlO₃:Bi. Furthermore, although

the optical transition between initial and final states being contributed equally by two Bi ions is not likely to be the emission observed experimentally in GdAlO₃:Bi, such a transition is dominating in hexagonal boron nitride luminescence [21], where the ground state and excited state of C_BC_N pair are localized in close proximity and exhibit a smaller Stokes shift than that of the common donor-acceptor pair. Furthermore, the study of Bi pairs in GdAlO₃ perovskite can provide insight into the excited-state properties of the polaron pairs, where an electron polaron and a hole polaron localize on two adjacent metal-halogen octahedral in the Pb²⁺ or Sn²⁺-based halide perovskites [22] with ns² lone-pair electrons.

Due to similar geometric structure and chemical properties, and similar Bi pair excited-state structures and stabilities (Table S11 and Table S12 in the SM [29]), the excitation and emission energies are predicted to be similar in YAlO₃:Bi but have not been observed experimentally. In 2006, Setlur *et al.* observed a visible emission around 420 and 470 nm in (Y, Gd)₃(Al, Ga)₅O₁₂:Bi, whose emission intensities increase with the concentrations of Gd³⁺ ions along with 0, 25, and 100%; meanwhile, there is no such type of visible emission in pure Y₃Ga₅O:Bi [46]. It has been long known that the phenomenon of “Gd³⁺ bridges” is important in energy migration from a sensitizer to an activator [47,48]. In GdAlO₃, the ⁸S_{7/2} → ⁶P_{7/2} transition of Gd³⁺ ions overlaps with the A-band emission of isolated Bi³⁺. Due to the forbidden nature of *f-f* transitions of Gd³⁺, the upper excited state of Gd³⁺ shows sufficiently long lifetime and does not relax noticeably by a multiphonon process. The abundant Gd³⁺ ions in hosts, with nearby distance at around 3.7 Å, can act as bridges to migrate the energy from an excited Bi ion via Gd³⁺ to excite the Bi-Bi pair to its $\text{Bi}_R^- - \text{Bi}_R^+$ excited states, which produces the 495-nm emission after excited-state structure relaxation. The excitation, energy migration, and emission are plotted schematically in Fig. 10. No such type of pair emission is observed in YAlO₃:Bi, consistent with the lack of tendency of forming excessive pairs and nonexistence of such energy migration bridges to the very dilute naturally present pairs. To sum up, the calculation results do not support the pairing via the Bi-O-Bi linkages in GdAlO₃:Bi [3], but support the mechanism of Bi³⁺ pair emission due to Gd-bridged energy migration reported in (Y, Gd)₃(Al, Ga)₅O₁₂:Bi.

IV. CONCLUSION

The trap levels and photoluminescence of Bi dopants in a series of RBO₃ perovskites, including RAlO₃ (R = Y, Gd, La) and LaBO₃ (B = Al, Ga, In), are studied based on the first-principles calculations. The formation energies show that Bi dopants predominantly occupy the R site in the form of

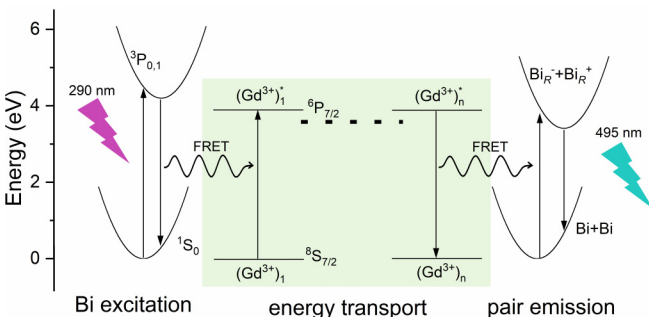


FIG. 10. Schematic Bi³⁺ pair emission mechanism of GdAlO₃:Bi.

Bi^{3+} ions series of perovskite oxides under normal fabrication conditions. Different R or B cations result in the variation of the energy band edges, and thus the differences of trap levels and photoluminescence of Bi_R^0 defects (Bi^{3+} dopant ions). And, the corresponding electron traps are all around -4 eV relative to the vacuum level, whereas the trap depths vary with the shift of CBM in different hosts. The hole trap depths exhibit obvious trends with the variation of R -O bond lengths rather than those of Bi_R -O. In LaAlO_3 , due to the longer Bi -O bond length and weaker nephelauxetic effect, Bi_{La} does not have a hole trap level and its VRBE electron trap level is also higher than others. The lowest excited level that produces the photoluminescence is ${}^3P_{0,1}$ of Bi_R^0 (Bi^{3+}) in all the hosts considered, except in $\text{LaAlO}_3:\text{Bi}$, which is the valence band to Bi charge transfer state ($\text{Bi}_{\text{La}}^{1-} + h_{\text{VBM}}$). The transition energies involving ${}^3P_{0,1}$ state show a weak linear correlation to the band gaps of hosts with a slope about 0.22, and exhibit an almost constant Stokes shift of ~ 0.7 eV. Thus, the values of the A -band transition and the adiabatic MMCT or CT transitions can be estimated based on the band structure and transition-level calculations of Bi-doped materials. Furthermore, the calculations show that there is no tendency of forming excessive Bi pairs in the hosts considered, which explains why the pair emission is not observed except for GdAlO_3 , where Gd^{3+}

ions work as bridges to migrate the energy from an excited Bi ion around and eventually to the extremely scarce $\text{Bi}_R^- - \text{Bi}_R^+$ (usually referred to as $\text{Bi}^{2+} - \text{Bi}^{4+}$) intervalence charge transfer state of the Bi_R^0 (Bi^{3+}) pair existing naturally as a consequence of random distribution. The results on Bi^{3+} ion-activated perovskite oxides provide insight in design and optimization of the performance of Bi^{3+} -activated or sensitized phosphors, for instance, by manipulating the excitation and emission wavelengths and trap depths via solid solution or ion codoping.

ACKNOWLEDGMENTS

The numerical calculations in this paper were partially performed on the supercomputing system in the Supercomputing Center of University of Science and Technology of China. This work was financially supported by the National Key Research and Development Program of China (Grants No. 2018YFA0306600 and No. 2016YFB0701001), China-Poland Intergovernmental Science and Technology Cooperation Program, Grant No. 2020[15]/10, the National Natural Science Foundation of China (Grants No. 61635012, No. 11974338, No. 11974022, No. 11604002, and No. 21805082), and University Science Research Project of Anhui Province (Grant No. KJ2017A791).

-
- [1] J. D. Majher, M. B. Gray, T. A. Strom, and P. M. Woodward, *Chem. Mater.* **31**, 1738 (2019).
- [2] Y. Wei, G. C. Xing, K. Liu, G. G. Li, P. P. Dang, S. Liang, M. Liu, Z. Y. Cheng, D. Y. Jin, and J. Lin, *Light-Sci. Appl.* **8**, 15 (2019).
- [3] A. M. Srivastava and H. A. Comanzo, *Opt. Mater.* **63**, 118 (2017).
- [4] A. Krasnikov, L. Lipinska, E. Mihokova, M. Nikl, T. Shalapska, A. Suchocki, S. Zazubovich, and Y. Zhydachevskii, *Opt. Mater.* **36**, 1705 (2014).
- [5] T. K. V. Rao, C. S. Kamal, T. Samuel, V. S. Rao, V. S. Rao, P. V. S. S. N. Reddy, and K. R. Rao, *J. Mater. Sci.-Mater. Electron.* **29**, 1011 (2018).
- [6] A. M. Srivastava, *Mater. Res. Bull.* **34**, 1391 (1999).
- [7] W. Zhang, Y. Tong, F. Hu, R. Wei, L. Chen, and H. Guo, *Ceram. Int.* **47**, 284 (2021).
- [8] B. Yuan, Y. Song, L. Kong, C. Dai, and H. Zou, *Physica B* **550**, 75 (2018).
- [9] P. Dang, D. Liu, G. Li, A. A. Al Kheraif, and J. Lin, *Adv. Opt. Mater.* **8**, 1901993 (2020).
- [10] J. Xue, X. Wang, J. H. Jeong, and X. Yan, *Phys. Chem. Chem. Phys.* **20**, 11516 (2018).
- [11] B. Luo, F. Li, K. Xu, Y. Guo, Y. Liu, Z. Xia, and J. Z. Zhang, *J. Mater. Chem. C* **7**, 2781 (2019).
- [12] L. Wang, Q. Sun, Q. Liu, and J. Shi, *J. Solid State Chem.* **191**, 142 (2012).
- [13] T. Lyu and P. Dorenbos, *Chem. Mater.* **32**, 1192 (2020).
- [14] X. Yang, R. Zhao, Y.-H. Ji, H. Shi, and M.-H. Du, *Phys. Rev. Materials* **4**, 064604 (2020).
- [15] X. Huang, Z. Qiao, Z. Qiu, N. Ma, J. Wen, and L. Ning, *Inorg. Chem.* **59**, 16760 (2020).
- [16] X. Huang, Z. Qiao, J. Wen, and L. Ning, *J. Phys. Chem. C* **124**, 13400 (2020).
- [17] B. Lou, J. Wen, J. Cai, Y.-Y. Yeung, M. Yin, and C.-K. Duan, *Phys. Rev. B* **103**, 075109 (2021).
- [18] R. H. P. Awater and P. Dorenbos, *J. Lumin.* **184**, 221 (2017).
- [19] P. Boutinaud, *J. Lumin.* **197**, 228 (2018).
- [20] Z. Wang, S. C. Su, M. Younas, F. C. C. Ling, W. Anwand, and A. Wagner, *RSC Adv.* **5**, 12530 (2015).
- [21] M. Mackoitis-Sinkeviciene, M. Maciaszek, C. G. Van de Walle, and A. Alkauskas, *Appl. Phys. Lett.* **115**, 212101 (2019).
- [22] H. Shi, D. Han, S. Chen, and M.-H. Du, *Phys. Rev. Materials* **3**, 034604 (2019).
- [23] J. P. Perdew, A. Ruzsinszky, G. I. Csonka, O. A. Vydrov, G. E. Scuseria, L. A. Constantin, X. Zhou, and K. Burke, *Phys. Rev. Lett.* **100**, 136406 (2008).
- [24] G. Kresse and J. Furthmuller, *Phys. Rev. B* **54**, 11169 (1996).
- [25] G. Kresse and D. Joubert, *Phys. Rev. B* **59**, 1758 (1999).
- [26] P. E. Blochl, *Phys. Rev. B* **50**, 17953 (1994).
- [27] C. Freysoldt, B. Grabowski, T. Hickel, J. Neugebauer, G. Kresse, A. Janotti, and C. G. Van de Walle, *Rev. Mod. Phys.* **86**, 253 (2014).
- [28] T. R. Durrant, S. T. Murphy, M. B. Watkins, and A. L. Shluger, *J. Chem. Phys.* **149**, 024103 (2018).
- [29] See Supplemental Material at <http://link.aps.org/supplemental/10.1103/PhysRevB.104.115101> for the details of the charge corrections, the structures of the ground and excited states of the luminescence center, the vacuum referenced binding energies of the defects, the excited state structures, and energies of $\text{Bi}_{\text{R}0}(\text{Bi}^{3+})$ pairs.
- [30] T. Yamamoto and T. Mizoguchi, *Phys. Rev. B* **86**, 094117 (2012).

- [31] J. P. Perdew, M. Ernzerhof, and K. Burke, *J. Chem. Phys.* **105**, 9982 (1996).
- [32] J. He and C. Franchini, *Phys. Rev. B* **86**, 235117 (2012).
- [33] M. Gerosa, C. E. Bottani, L. Caramella, G. Onida, C. Di Valentin, and G. Pacchioni, *Phys. Rev. B* **91**, 155201 (2015).
- [34] P. Dorenbos, *Phys. Rev. B* **87**, 035118 (2013).
- [35] G. R. Remya, S. Solomon, J. K. Thomas, and A. John, *Mater. Today: Proc.* **2**, 1012 (2015).
- [36] S. Tiwari, R. K. Tamrakar, K. Upadhyay, and C. S. Robinson, *Bull. Mater. Sci.* **42**, 181 (2019).
- [37] H. B. Premkumar, B. S. Ravikumar, D. V. Sunitha, H. Nagabhushana, S. C. Sharma, M. B. Savitha, S. M. Bhat, B. M. Nagabhushana, and R. P. S. Chakradhar, *Spectrochim. Acta, Part A* **115**, 234 (2013).
- [38] L. Ning, W. Cheng, C. Zhou, C.-K. Duan, and Y. Zhang, *J. Phys. Chem. C* **118**, 19940 (2014).
- [39] M. Fu, T. Liu, X. Lu, J. Li, and Z. Ma, *Comput. Mater. Sci.* **141**, 127 (2018).
- [40] K. Hoang, *Phys. Rev. Materials* **1**, 075404 (2017).
- [41] K. Hoang, *Phys. Rev. Materials* **1**, 075403 (2017).
- [42] P. Dorenbos, *J. Phys.: Condens. Matter* **25**, 225501 (2013).
- [43] P. Dorenbos, *Phys. Rev. B* **62**, 15640 (2000).
- [44] X. Li, P. L. Li, Z. J. Wang, S. M. Liu, Q. Bao, X. Y. Meng, K. L. Qiu, Y. B. Li, Z. Q. Li, and Z. P. Yang, *Chem. Mater.* **29**, 8792 (2017).
- [45] Z. Feng, B. Lou, M. Yin, Y.-Y. Yeung, H.-T. Sun, and C.-K. Duan, *Inorg. Chem.* **60**, 4434 (2021).
- [46] A. A. Setlur and A. M. Srivastava, *Opt. Mater.* **29**, 410 (2006).
- [47] P. A. Tanner, L. Zhou, C.-K. Duan, and K.-L. Wong, *Chem. Soc. Rev.* **47**, 5234 (2018).
- [48] H. Zhang, Z.-H. Chen, X. Liu, and F. Zhang, *Nano Res.* **13**, 1795 (2020).
- [49] A. Mondal and J. Manam, *Ceram. Int.* **46**, 23972 (2020); P. R. Slater, J. T. S. Irvine, T. Ishihara, and Y. Takita, *Solid State Ionics* **107**, 319 (1998).
- [50] S. Kumar, G. D. Dwivedi, A. G. Joshi, S. Chatterjee, and A. K. Ghosh, *Mater. Char.* **131**, 108 (2017).